ОБЪЕДИНЕННЫЙ
ИНСТИТУТ
ЯДЕРНЫХ
ИССЛЕДОВАНИЙ

Дубна

E1-2003-22

J. A. Budagov, J. I. Khubua[1], Y. A. Kulchitsky[2],
N. A. Russakovich, R. Stanek[3], V. B. Vinogradov

ELECTRON AND PION CALIBRATIONS OF THE **ATLAS TILECAL** MODULES (September 2001 Test Beam)

Presented at the International ATLAS Collaboration Conference, February 2002, CERN, Geneva, Switzerland

[1]Permanent address: TSU HEPI, Tbilisi, Georgia
[2]Permanent address: B. I. Stepanov Institute of Physics, National Academy of Sciences, Minsk, Belarus
[3]Argonne National Laboratory, USA

2003

1 Introduction

The constructed ATLAS detector at the LHC will have the great physics discovery potential, in particular in the detection of a heavy Higgs boson [1, 2]. Calorimeters will play a crucial role in it.

The key question of calorimetry is the absolute energy calibration. The physics goals have led to the following requirement for the knowledge of the absolute scale of energy: in the case of hadronic jets, the scale should be known to an accuracy of 1% [3].

The other important issue is the energy linearity. The most stringent linearity requirements for the hadronic calorimeter come from the study of quark compositness where the jet energy scale has to be linear within 2% up to the transverse energy of 4 TeV [4].

The ATLAS hadronic TILECAL calorimeter will contain 5120 cells which will be read-out by 10240 PMT's [5]. The energy deposited in a single cell can vary from 15 MeV to 1.5 TeV. For each cell the calibration constants, which define the relationship between the calorimeter signals, expressed in picoCoulombs, and the energy of the absorbed particles, which produced the signals, must be determined.

The intercalibration (the minimization of the channel-to-channel variation of calibration constants) and monitoring is realized by the Cesium Monitoring System [6] in which a capsule containing Cs^{137} γ-source [7] are carried along by a liquid flow inside calibration tubes piercing through all the cells of the calorimeter.

This work is devoted to the determination of the electron and pion calibration constants of the cells of two extended barrel modules of this calorimeter on the basis of the September 2001 test beam period.

2 The setup

The setup is the following (Fig. 1). The Barrel Module 0 is the bottom module mounted on the table. The middle layer is the production barrel module JINR-34. The top layer is the two extended barrel modules: IFA015 for $\eta > 0$ (beam left) (EBM+) and IFA024 for $\eta < 0$ (beam right) (EBM−). As to the electronics readout that only the extended barrel modules had production drawers.

The layout of the readout cell geometry for this setup is shown in Fig. 2. Each cell is a set of scintillating tiles connected by fibers to 2

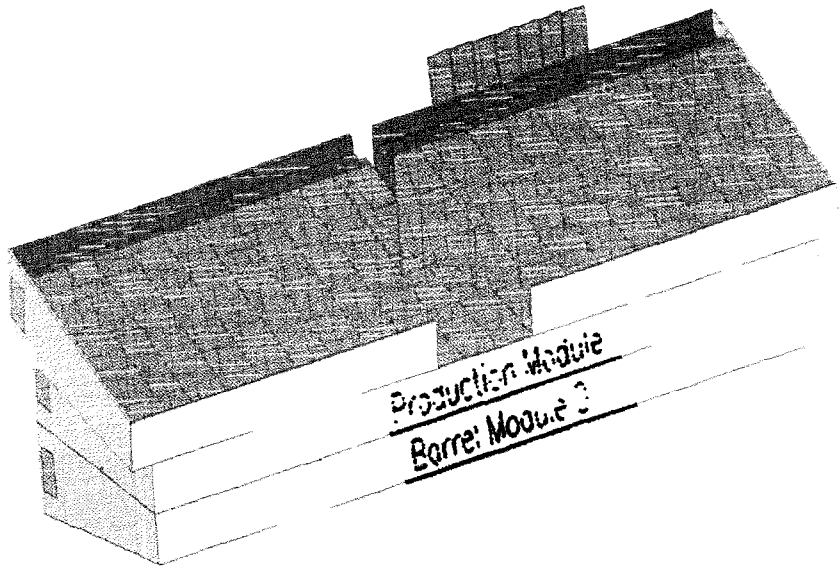

Figure 1: Sketch of the September 2001 test beam setup.

PMTs. There are 11 transverse rows of tiles (tilerows) in a module. A−16 cell has tilerows 1 - 3, B−15 cell — 4 - 7, D−6 cell — 8 - 11.

This setup has been installed on the H8 beam line of the CERN SPS. Beam quality and geometry have been monitored with a set of the scintillation counters and the beam chambers. Two threshold Cherenkov counters have allowed to tag electrons, pions and protons.

3 Data Taking and Event Selection

The analyzed runs and the corresponding beam energies are the following: 20 GeV — 120509 ÷ 120540 runs, 50 GeV — 120406 ÷ 120460 runs, 180 GeV — 120255 ÷ 120347 runs. The volume of the analyzed information is 100 ntuples, 4 million events, 24 Gbyte.

The following cuts were used for the event selection. The cuts of the amplitudes of the scintillation counters are: $300 < S_1 < 3000$, $300 < S_2 < 2000$, $300 < S_3 < 1000$. The cuts of the beam chambers coordinates are: $-15 < X_1 < 10\ mm$, $-20 < Y_1 < 10\ mm$, $-20 < X_2 < 15\ mm$, $-25 < Y_2 < 20\ mm$, $-25 < X_{imp} < 20\ mm$, $-40 < Y_{imp} < 20\ mm$, $-20 < (X_1 - X_2) < 20\ mm$, $-30 < (Y_1 - Y_2) < 25\ mm$.

The distributions of events as a function of these variables are shown in Fig. 3 and Fig. 4.

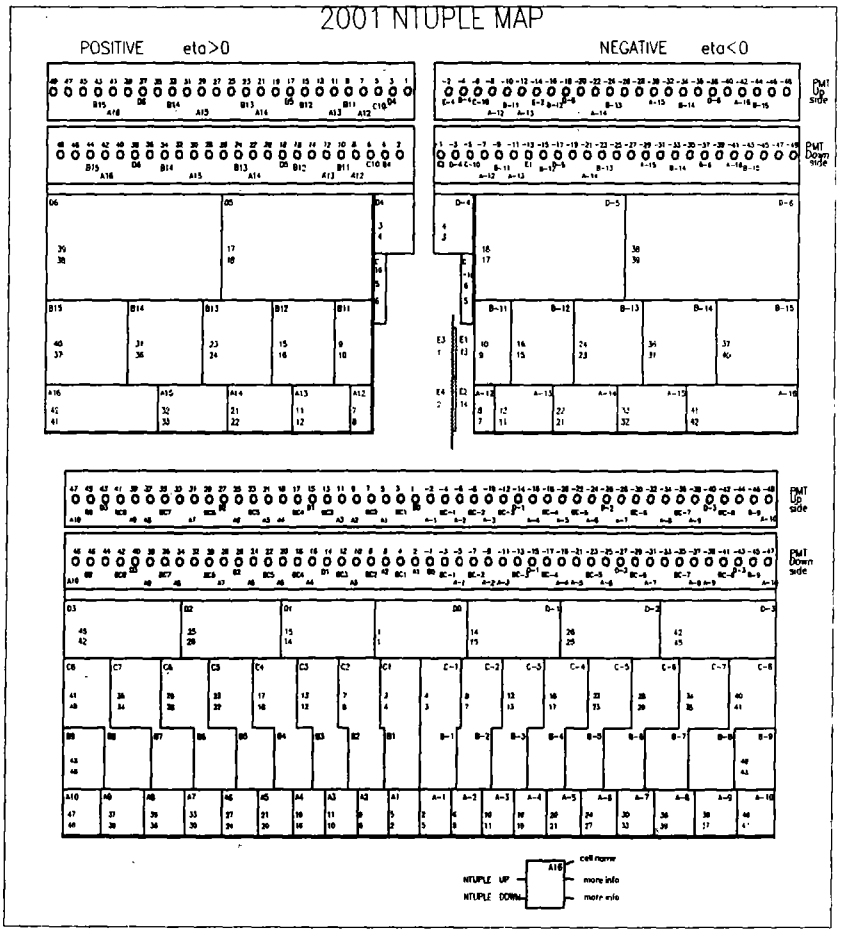

Figure 2: The layout of the cell geometry.

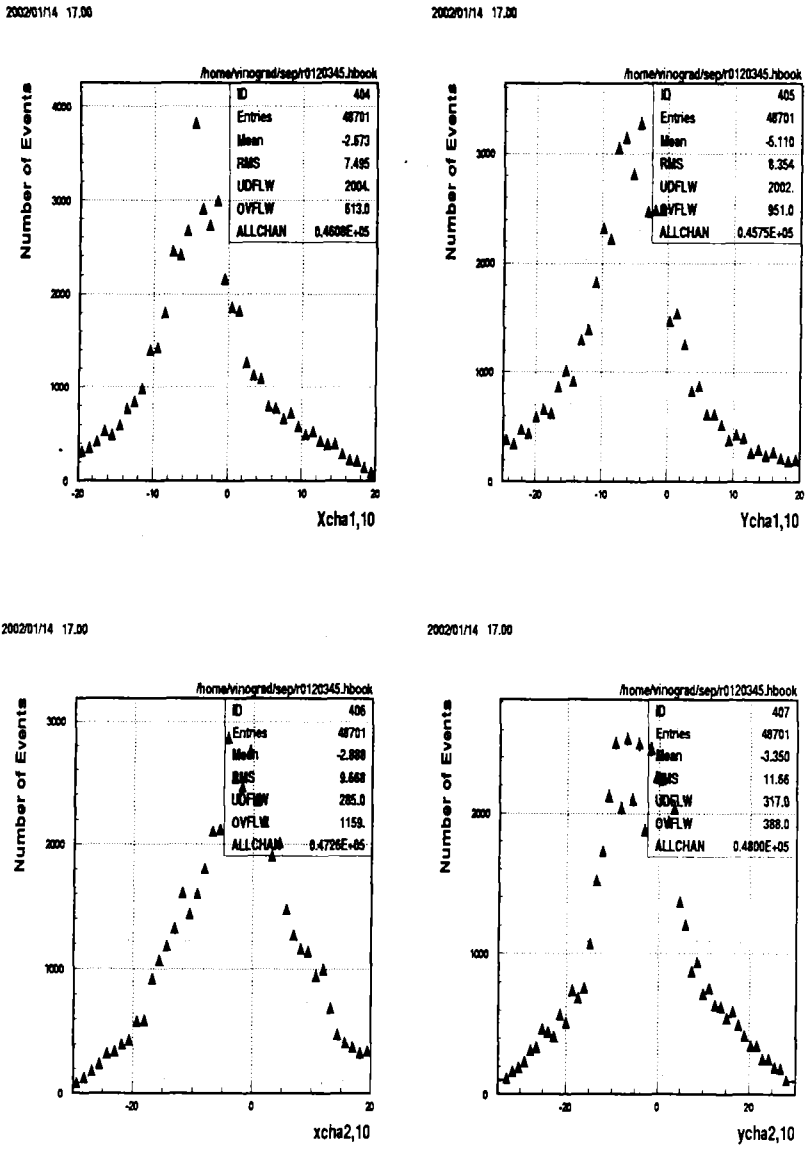

Figure 3: The distributions of the beam chambers coordinates X_1, Y_1, X_2, Y_2.

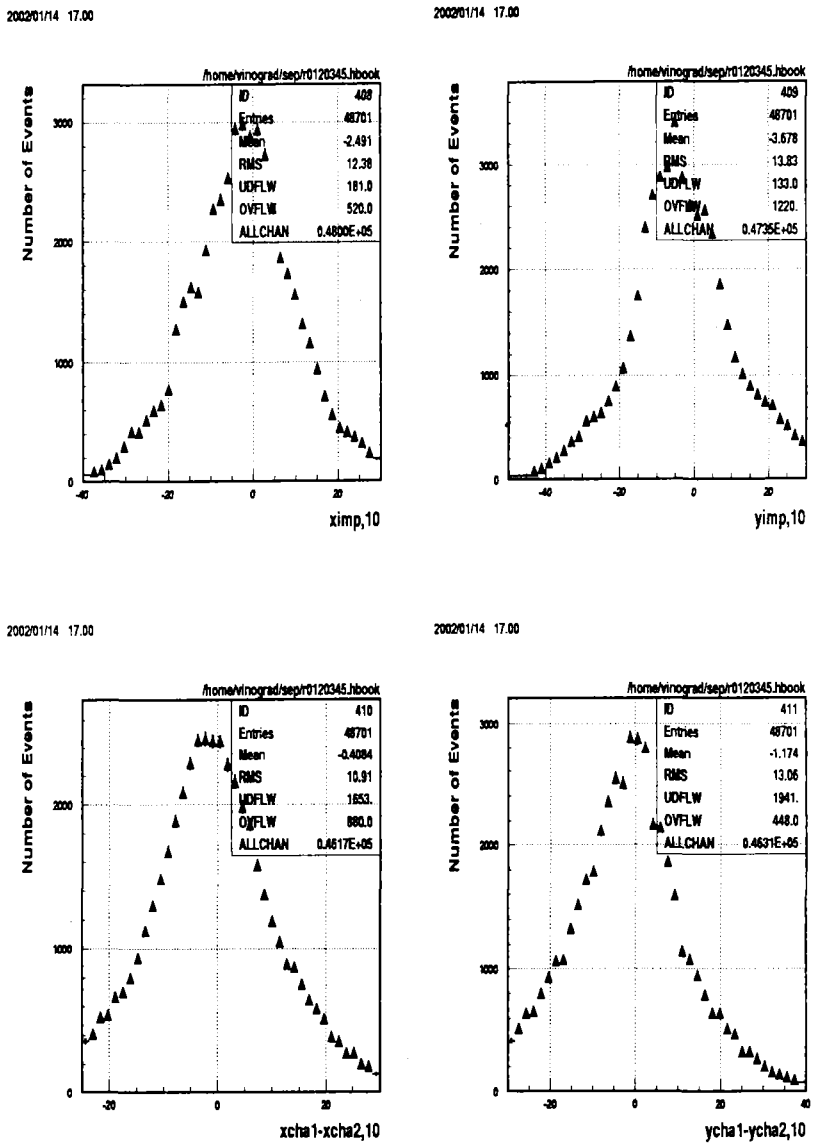

Figure 4: The distributions of the beam impact point coordinates X_{imp} and Y_{imp} and the differences of the beam chambers coordinates $(X_1 - X_2)$ and $(Y_1 - Y_2)$.

4 Identification of electron and pion events

There are several methods for identification of electron and pion events, in particular Neural Networks [8].

We have estimated that in order to have the systematic error in the electron calibration constant due to the pion contamination smaller than 0.3% this contamination must be smaller than 1.5% in the energy range of 20 - 180 GeV.

We have used the following cuts for the electron selection: the cut 1 is $C_i > 0.9 \div 1.0$, the cut 5 is $E_{cut} > 0.12 \div 0.14$, the cut 6 is $\check{C}_1 > 400$.

The cut 4 is the relative shower energy deposition in the first two calorimeter depths:

$$C_i = \sum_{selected\ i} \sum_{j=3} \sum_{k=1}^{2} \sum_{l=1}^{2} E_{ijkl}/E_{beam} \ . \qquad (1)$$

The indexes i and k in E_{ijkl} determine the regions of electromagnetic shower development.

The basis for this electron-hadron separation is the different longitudinal energy deposition for electrons and hadrons. For example, if a 100 GeV particle crosses 45 cm of the Tile calorimeter from the front face it corresponds to 18 radiation lengths or 2.2 nuclear interaction lengths. The amount of the deposited energy is equal to 95% for the electromagnetic shower and 50% for the hadronic shower [9].

The cut 5

$$E_{cut} = \frac{\sqrt{\sum_c (E_c^\alpha - \sum_c E_c^\alpha / N_{cell})^2}}{\sum_c E_c^\alpha} \ , \qquad (2)$$

where $1 \leq c \leq N_{cell}$, N_{cell} is the used cells number, $\alpha = 0.6$, is related with the lateral shower spread. For example, for the 100 GeV hadronic shower the 99% containment radius is equal to 430 mm, but for the electromagnetic shower the one is equal to 70 mm [9].

The cut 6 is connected with the first Cherenkov counter amplitude and used for $E_{beam} = 20\ GeV$.

For the muon rejection we have used the cut in the total deposited energy: 2 (10, 100) GeV $< E_{tot} <$ 30 (70, 220) GeV for energies 20 (50, 180) GeV. This cut effectively selects muons as muons loose a very small fraction of their energy in the calorimeter [10].

Fig. 5 shows the C_i and E_{cut} distributions for E = 180 GeV, EBM−, $\theta = +20^o$, A−16. The left peak corresponds to the pion events, the

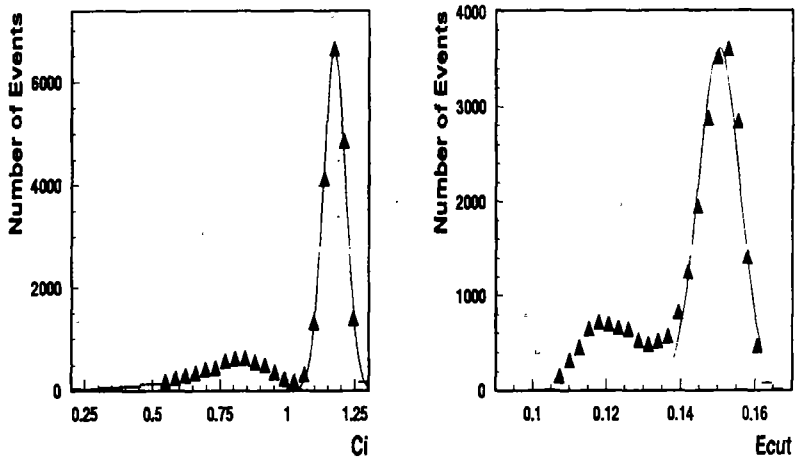

Figure 5: The C_i and E_{cut} distributions for $E = 180$ GeV.

right peak — the electron events. Fig. 6 shows the typical C_i and E_{cut} distributions. The left peak corresponds to the pion events, the right peak — the electron events.

Fig. 7 shows the typical scatter plots of E_{cut} vs C_i, E_{cut} vs $\check{C}_1$ and C_i vs $\check{C}_1$. The top right regions are the electron events, the bottom left regions are the pion events. These Figures allow to determine the values of the cuts and to estimate the contaminations.

At energies $\leq$ 20 GeV there is a bad separation with the C_i and E_{cut} (contaminations about 10%). This situation is greatly improved by using the first Cherenkov counter signal cut. Fig. 6 shows the C_i and E_{cut} distributions for E = 20 GeV without using the Cherenkov counter signal (top) and with the one (bottom). As can be seen after using the first Cherenkov counter cut for the E = 20 GeV events the pion contamination becomes negligible.

We have estimated by extrapolation of the fitted pion peak curve to the region of the electron peak (Figs. 5) that the contamination of the pion events in the electron events does not exceed the 0.2% level. The developed method has allowed to decide the task of obtaining of the clean samples of the electron and pion events for the calibration of modules of the tile calorimeter.

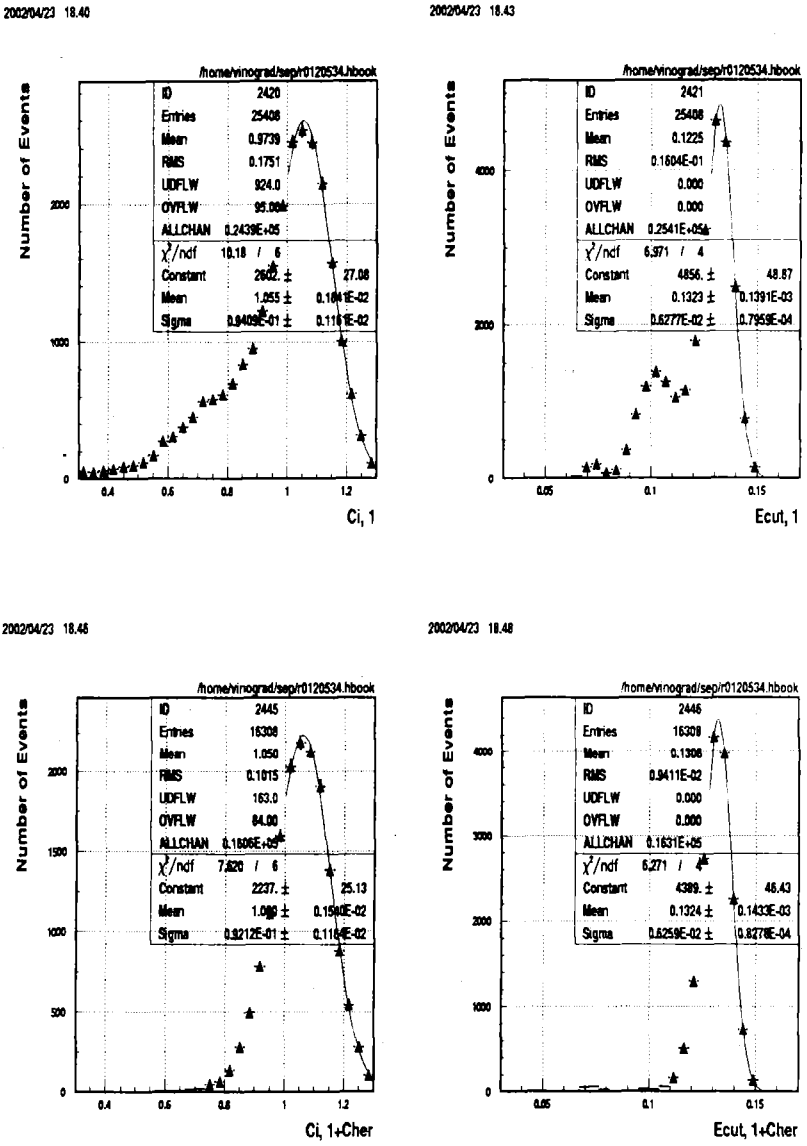

Figure 6: The C_i and E_{cut} distributions for E = 20 GeV, EBM−, $\theta = -20^o$, A−14 without using of the first Cherenkov counter signal (top) and with the one (bottom).

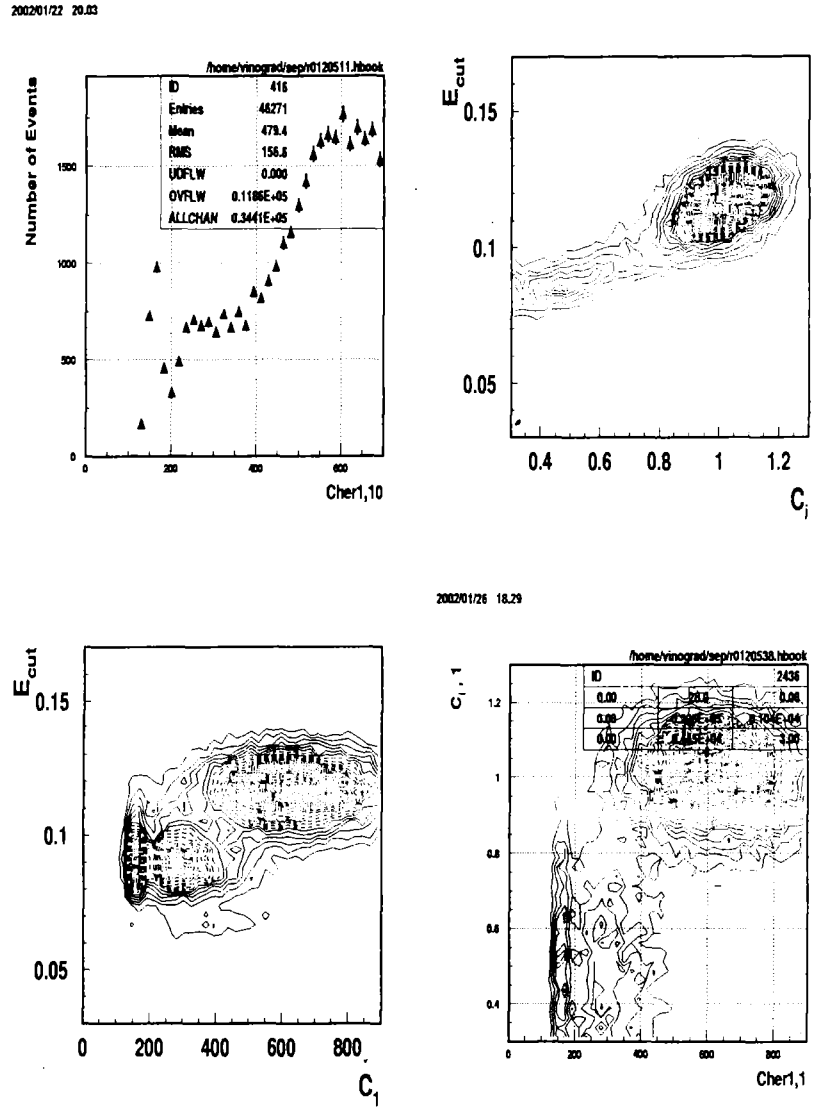

Figure 7: The distribution of the first Cherenkov counter amplitude (top – left) and the scatter plots of E_{cut} vs C_i (top – right), E_{cut} vs $\check{C}_1$ (bottom – left) and C_i vs $\check{C}_1$ (bottom – right) for $E = 20\ GeV$, EBM+, $\theta = -20°$, A$-$12.

5 Electron Calibration

5.1 Electron Calibration at $\theta = \pm 20^o$

The electron response in our calorimeter is a function of E_{beam}, Θ and Z [11]. The energy spectrum for a given run (the beam has the transversal spread ± 20 mm on a face of a module (Fig. 4)) as a rule is non – Gaussian (Fig. 8).

Earlier the mean normalized electron responses as a function of Z coordinate have been well described by the sine function [11]:

$$f(Z) = P_2 + P_1 \sin(2\pi Z/P_3 + P_4). \quad (3)$$

But it is not the case for the August and September 2001 testbeam.

Fig. 9 shows the electron response as a function of Z for 180 GeV.

As can be seen, the sine function behaviour is absent. This may be explained by the existence in the beam channel some incidental thing (a scintillation counter turned to 90^o angle) which causes the essential γ-quanta bremsstrahlung. When this counter have been removed (for 20 – 50 GeV runs, $N_{run} > 120400$) the sine behaviour appeared (Fig. 10).

Fig. 11 shows how the amplitude distribution of the S_1 scintillation counter changes when this incidental thing is being (the left picture, the wide bump in the range of 1000 – 2000 counts, caused by γ-quantas, is observed) and removed (the right picture).

The calibration constants (the mean normalized electron responses), extracted from the distributions of E_e/E_{beam} as a function of impact point Z coordinate, for each A-cell, each energy and angle are shown in Fig. 12 for cells of EBM– and Fig. 13 for EBM+ and given in Table 1. Their spreads as a function of a cell are ± 2 % for EBM– and ± 3 % for EBM+ except the A–14 cell ($\theta = +20^o$) of EBM+, where the normalized electron response differs by 8% from the average.

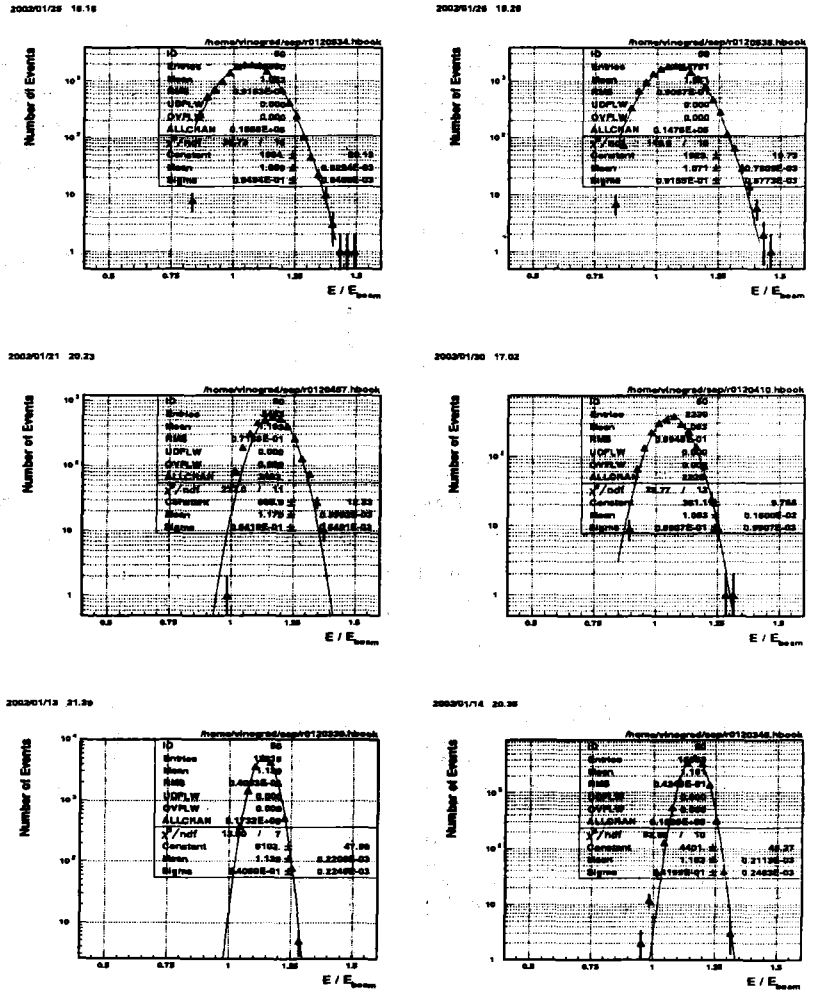

Figure 8: The electron energy distributions for $E = 20\ GeV$, EBM−, $\theta = -20^o$, A−14 (up-left), for $E = 20\ GeV$, EBM+, $\theta = -20^o$, A−13 (up-right), for $E = 50\ GeV$, EBM−, $\theta = +20^o$, A−13 (middle-left), for $E = 50\ GeV$, EBM+, $\theta = +20^o$, A−12 (middle-right), for $E = 180\ GeV$, EBM−, $\theta = -20^o$, A−14 (down-left) and for $E = 180\ GeV$, EBM+, $\theta = -20^o$, A−12 (down-right).

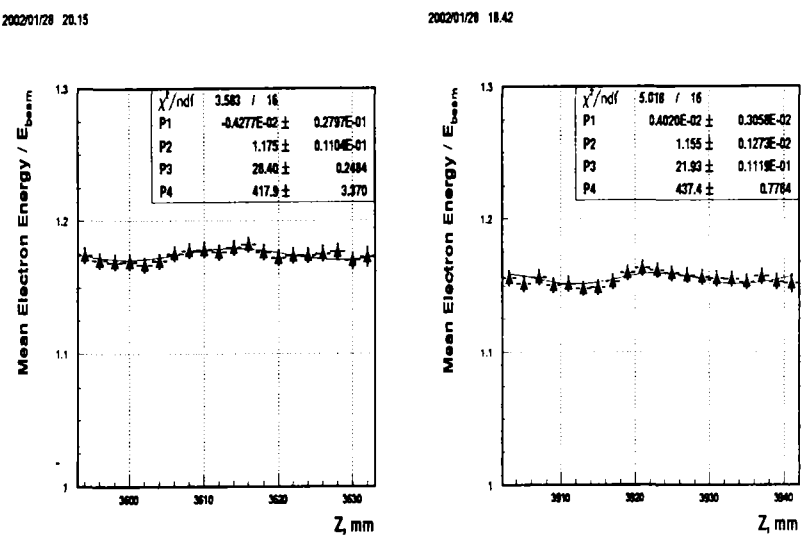

Figure 9: The normalized electron response (E_e/E_{beam}) for $E = 180\ GeV$, EBM$-$, $\theta = -20^o$, A$-$12 (left) and for $E = 180\ GeV$, EBM+, $\theta = +20^o$, A$-$13 (right) as a function of the impact point Z coordinate.

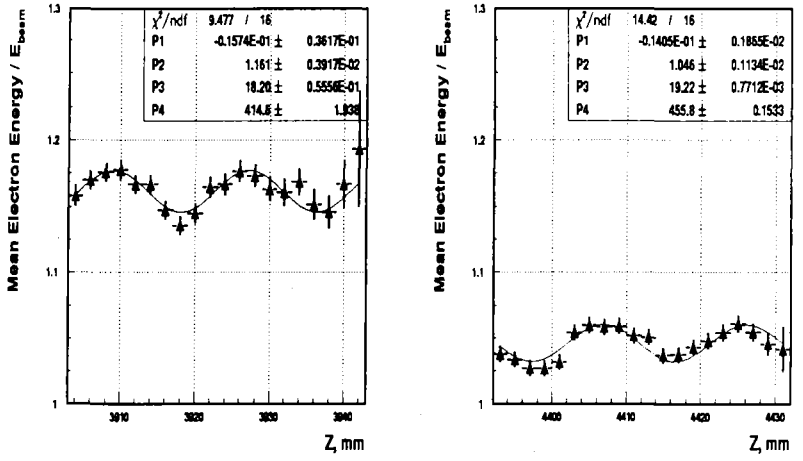

Figure 10: The normalized electron response (E_e/E_{beam}) for $E = 50\ GeV$, EBM$-$, $\theta = +20^o$, A$-$13 (left), for $E = 20\ GeV$, EBM+, $\theta = -20^o$, A$-$14 (right) as a function of the impact point Z coordinate.

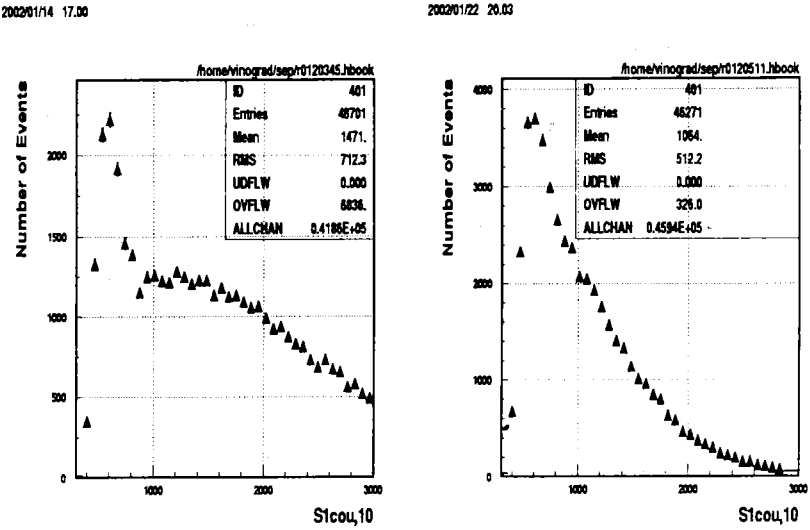

Figure 11: The amplitude distributions of the S_1 scintillation counter for $E = 180\ GeV$, EBM+, $\theta = -20^o$, A$-$12 (left), for $E = 20\ GeV$, EBM+, $\theta = +20^o$, A$-$15 (right).

Table 1: The calibration constants (pC/GeV) for the extended barrel modules: IFA015 (A+12 $\div$ A+16) and IFA024 (A$-$12 $\div$ A$-$16).

Cell	20 GeV		50 GeV	180 GeV	
	-20^o	$+20^o$	$+20^o$	-20^o	$+20^o$
A+12	1.071±0.002		1.161±0.001*	1.161±0.006	
A+13	1.010±0.002	1.047±0.002	1.145±0.002	1.093±0.001	1.155±0.001
A+14	1.046±0.002	1.013±0.001	1.060±0.006	1.125±0.002	1.075±0.003
A+15		1.166±0.003		1.179±0.002	
A+16		1.144±0.004		1.148±0.001	
mean	1.042±0.013	1.049±0.012	1.139 ±0.02	1.126±0.012	1.148±0.02
A$-$12		1.084±0.001	1.166±0.003		1.175±0.005
A$-$13	1.023±0.002	1.086±0.001	1.161±0.004		1.176±0.005
A$-$14	1.061±0.002	1.074±0.001	1.147±0.004	1.139±0.001	1.164±0.004
A$-$15	1.045±0.003	1.045±0.001	1.137±0.004	1.130±0.001	1.142±0.004
A$-$16	1.059±0.002	1.077±0.001		1.137±0.001	1.172±0.004
mean	1.050±0.005	1.072±0.008	1.155±0.006	1.135±0.002	1.164±0.003

* the calibration constant at -20^o

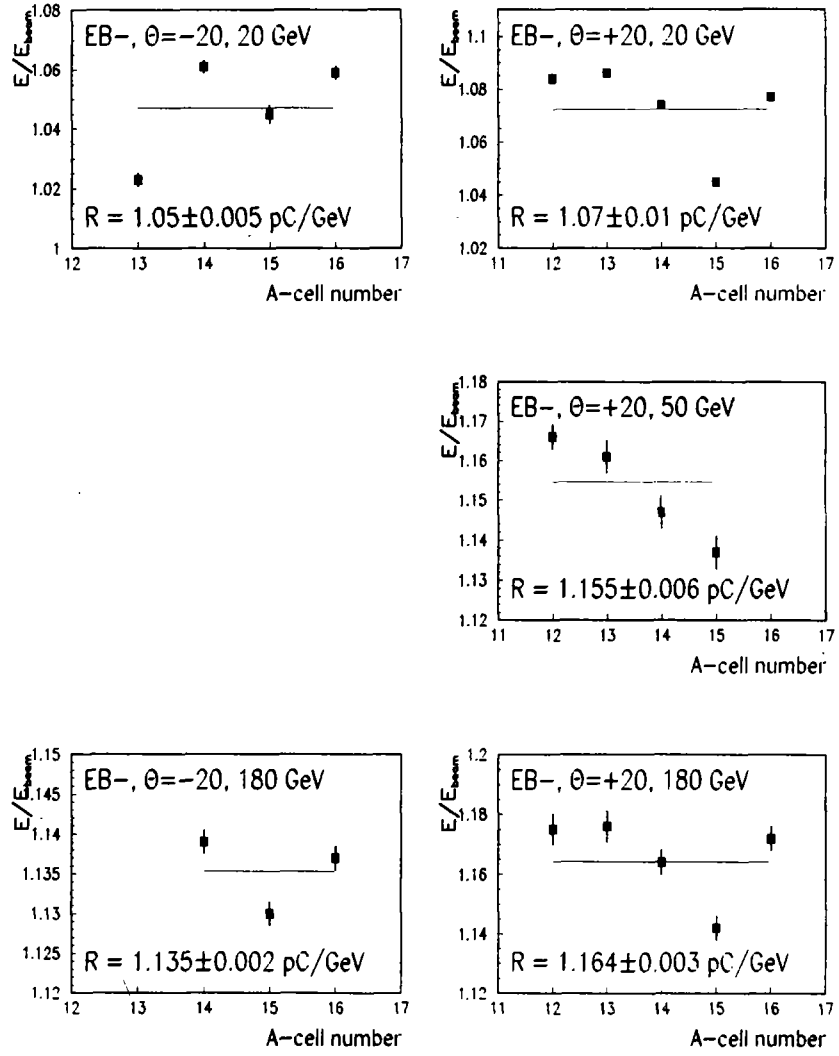

Figure 12: The calibration constants for the A-cells of EBM−: for $E = 20\ GeV$, $\theta = -20^o$ (top-left), for $E = 20\ GeV$, $\theta = +20^o$ (top-right), for $E = 50\ GeV$, $\theta = +20^o$ (middle-right), for $E = 180\ GeV$, $\theta = -20^o$ (bottom-left), for $E = 180\ GeV$, $\theta = +20^o$ (bottom-right).

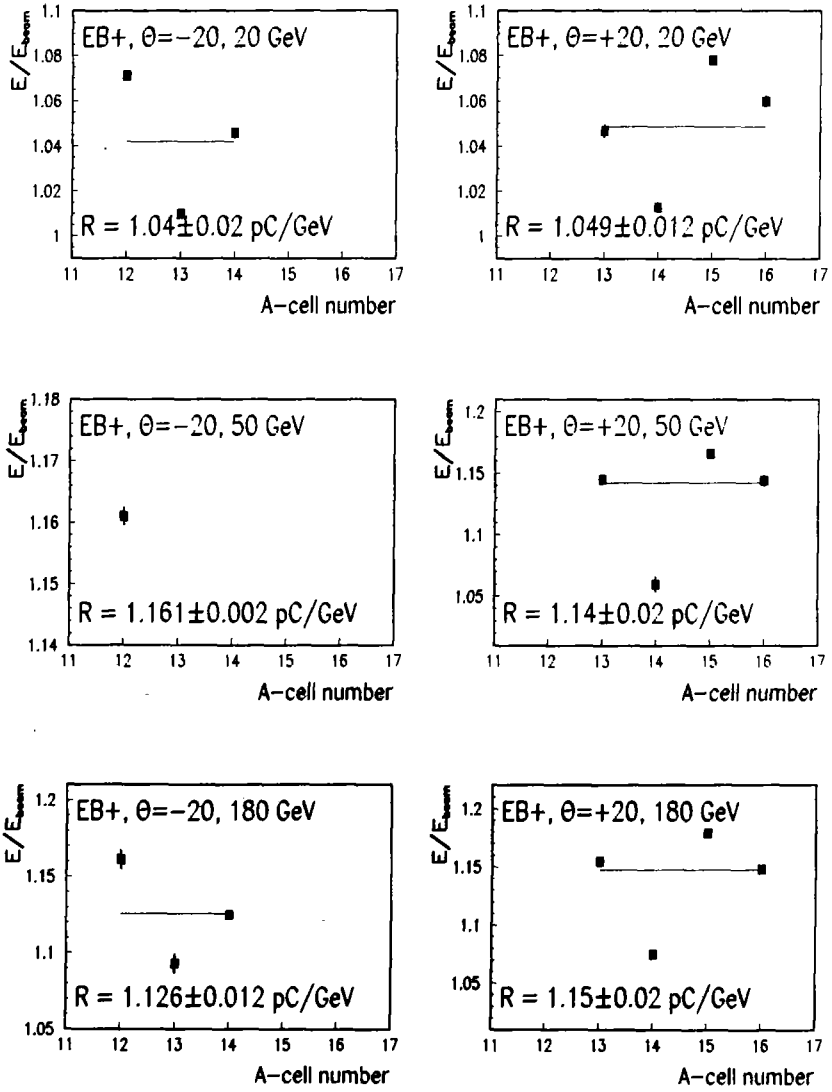

Figure 13: The calibration constants for cells of EBM+.

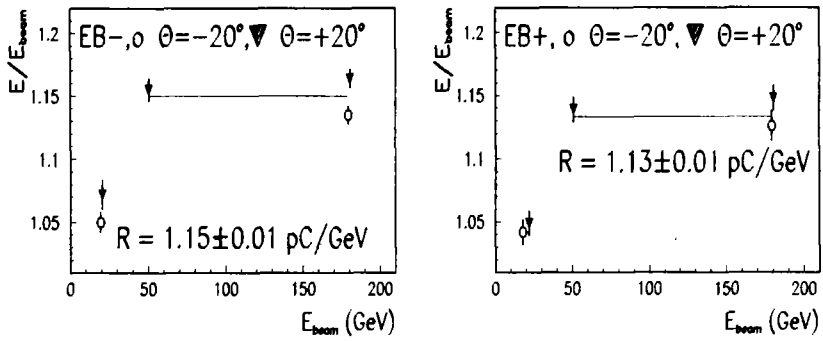

Figure 14: The average cell calibration constants for EBM− (left) and EBM+ (right) as a function of energy.

Fig. 14 shows the calibration constants averaged over cells for EBM− and EBM+ as a function of energy. As can be seen, the calibration constants for 20 GeV, corresponded to high gain, are about 10% less than the calibration constants for 50 and 180 GeV, corresponded to low gain. Perhaps, the real electron beam energy at 20 GeV was smaller of 10% than the nominal energy.

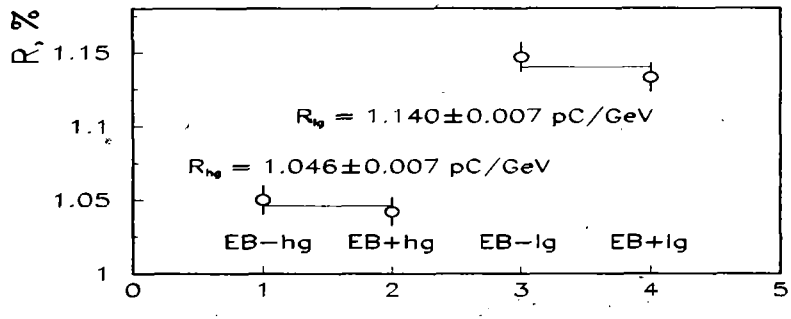

Figure 15: The low gain R_{lg} and high gain R_{hg} electron calibration constants.

Fig. 15 shows the low gain R_{lg} calibration constants, averaged over cells and over 50 and 180 GeV energies, and the high gain R_{hg} calibration constants for EBM− and EBM+. The obtained weighted averages are equal to 1.140 ± 0.007 pC/GeV for low gain and 1.046 ± 0.007 pC/GeV for high gain.

5.2 Electron calibration for various η

The normalized electron response (E_e/E_{beam}) as a function of η are shown in Fig. 16 and given in Table 2. The electron calibration constants for $\eta = -1.35$ are equal to 1.085±0.002 for 20 GeV and 1.143±0.004 for 50 GeV. The ones for 180 GeV are: for EBM−, $-1.35 < \eta < -1.05$ is 1.12 ± 0.01 pC/GeV, for EBM+, $1.05 < \eta < 1.35$ is 1.13 ± 0.01 pC/GeV.

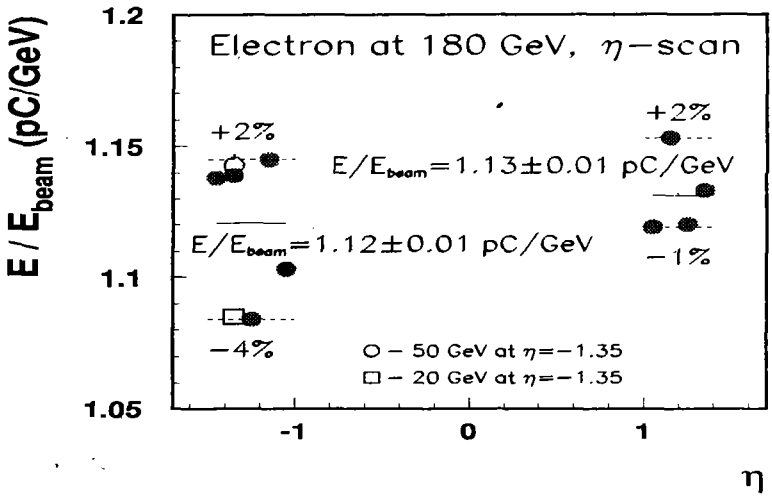

Figure 16: The electron calibration constants as a function of η.

Table 2: Calibration constants at 180 GeV for various η.

η	pC/GeV	η	pC/GeV
−1.05	1.103±0.001	+1.05	1.119±0.001
−1.15	1.145±0.001	+1.15	1.153±0.001
−1.25	1.084±0.001	+1.25	1.120±0.001
−1.35	1.139±0.001	+1.35	1.133±0.001
−1.45	1.138±0.001		

5.3 Electron Calibration at $\theta = 90^o$

The obtained electron calibration constants, C_e, in pC/GeV as a function of a tile number are shown in Fig. 17 and given in Table 3. Fig. 18 shows the comparison of the normalized ($R_i = C_{e_i} / < C_{e_i} >$) 180 and 20 GeV data. As can be seen, there is the coincidence in the behaviour of these values.

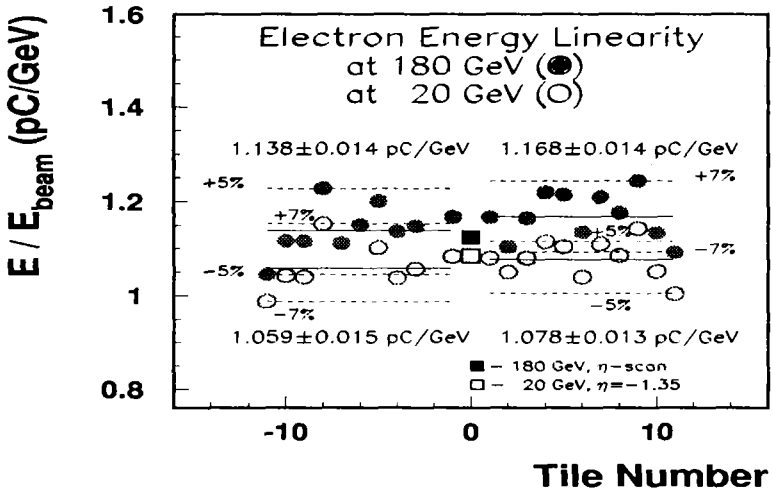

Figure 17: The electron calibration constants as a function of a tile number.

5.4 RMS of uniformity of cells and tilerows

The RMS values of uniformity of cells from the cell-to-cell comparison are given in Table 4 and of tilerows from the tilerow-to-tilerow comparison in Table 5. They have been calculated for electrons using the calibration constants presented in Tables 1, 2, 3 and for muons and Cs on the basis of the numerical values of responses shown in [12]. As can be seen, the Cs intercalibration of cells due to adjusting the HV of the corresponding PMTs is very good (smaller than 0.5%). The RMS values for the cell-to-cell uniformity for electrons are in the range of 1 – 2% and for muons the ones are about 1%. As to the RMS values for the tilerow-to-tilerow

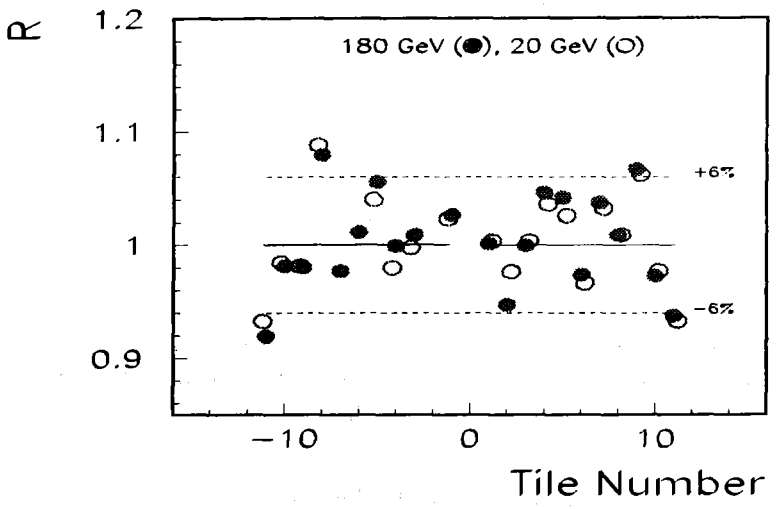

Figure 18: Comparison of the normalized 180 and 20 GeV data.

Table 3: The electron calibration constants in pC/GeV for various tiles at $\theta = 90°$.

Tile	EBM−		EBM+	
	20 GeV	180 GeV	20 GeV	180 GeV
1	1.084±0.002	1.168±0.002	1.080±0.002	1.167±0.002
2			1.051±0.002	1.104±0.002
3	1.057±0.002	1.148±0.002	1.080±0.002	1.165±0.002
4	1.038±0.002	1.137±0.002	1.115±0.002	1.219±0.002
5	1.102±0.002	1.201±0.002	1.104±0.002	1.214±0.002
6		1.151±0.002	1.040±0.002	1.135±0.002
7		1.112±0.002	1.111±0.002	1.209±0.002
8	1.153±0.002	1.228±0.002	1.086±0.002	1.176±0.002
9	1.040±0.002	1.116±0.002	1.143±0.002	1.243±0.002
10	1.043±0.002	1.117±0.002	1.052±0.002	1.134±0.002
11	0.988±0.002	1.046±0.002	1.004±0.002	1.093±0.002
mean	1.06±0.01	1.14±0.01	1.08±0.01	1.17±0.01

Table 4: Uniformity RMS (%) of cells from the cell-to-cell comparison.

	θ	EBM−	EBM+
Cs	90^o	0.1±0.1	0.3±0.1
electron	20^o	1.2±0.2	1.6±0.3
electron	90^o	1.2±0.5	1.8±0.7
muon	90^o	0.8±0.3	0.5±0.2

uniformity they equal to about 2% for the Cs data and 4% for electrons and muons. Note that the average internal tile-to-tile cell uniformity of modules obtained on the basis of Cs data is 6% [13].

Table 5: Uniformity RMS (%) of tilerows from the tilerow-to-tilerow comparison.

	θ	EBM−	EBM+
Cs	90^o	2.1±0.4	2.3±0.5
electron	90^o	4.6±0.8	3.9±0.6
muon	90^o	4.0±0.8	4.0±0.8

5.5 Comparison with the muon and Cs data

We have compared our electron data with the muon and Cs data [12]. The results of this comparison as a function of a tilerow number are shown in Figs. 19 and 20. Fig. 21 demonstrate the electron – muon and electron – Cs correlations. The correlation coefficients calculated as

$$q = \frac{\frac{1}{n-1}\sum_{i=1}^{n}(R_i^e - \overline{R^e})(R_i^b - \overline{R^b})}{s_e \cdot s_b}, \qquad (4)$$

where e – electron, $b = \mu,\ Cs$; R^e (R^b) is the normalized response, s_e (s_b) is the corresponding RMS, are given in Table 6. As can be seen, the strong correlations are observed. The straight line in Fig. 21 (right) obtained by fitting to the data represents the transfer function from the

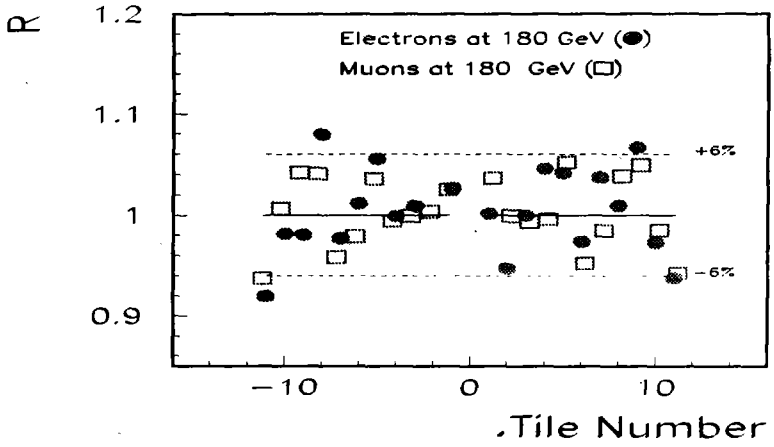

Figure 19: Comparison of the normalized 180 GeV electron and muon data.

Cs calibration to the electron one. Thus, the possibility to determine the electron calibration constants from the Cs calibration data has been demonstrated.

Table 6: The electron – muon and electron – Cs correlations.

	e – μ	e – Cs
EBM–	0.74±0.15	0.70±0.17
EBM+	0.65±0.18	0.58±0.21
all	0.70±0.12	0.64±0.13

6 Electron Energy Resolution

6.1 Energy Resolution for $\theta = \pm 20^o$

The mean relative electron energy resolutions, σ/E, extracted from the distributions of RMS/E as a function of the impact point Z coordinate for each A-cell and each energy and angle (Fig. 22), are shown in Fig. 23

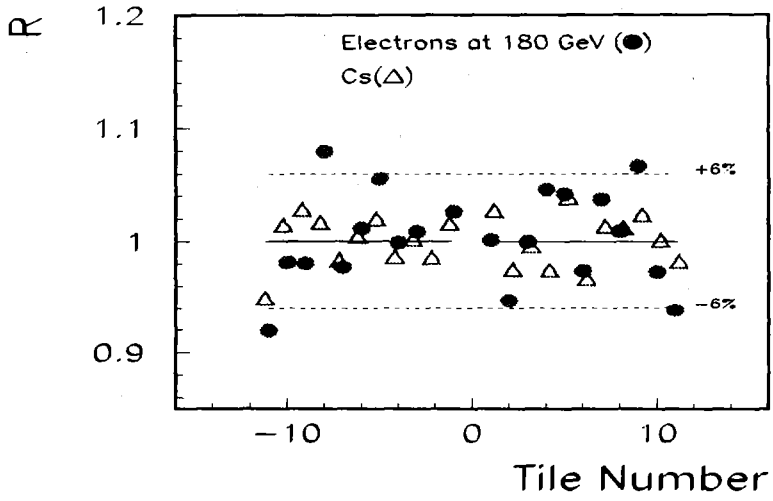

Figure 20: The comparison of the normalized 180 GeV electron data and the Cs data.

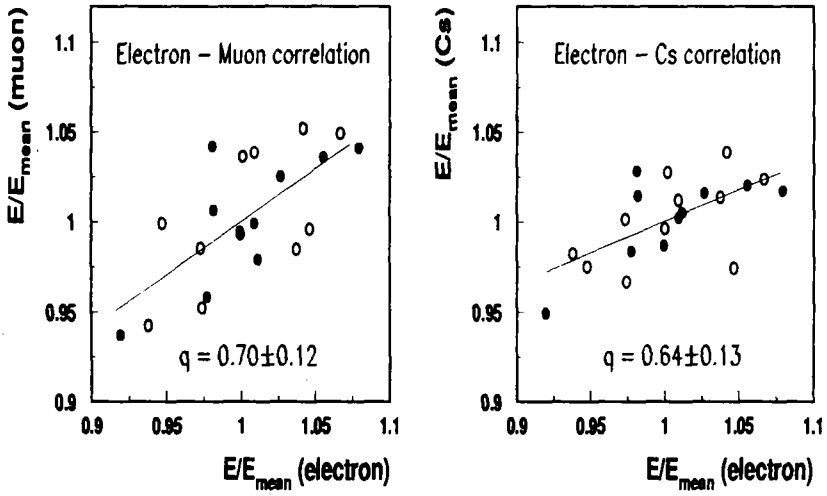

Figure 21: The electron – muon (left) and electron – Cs (right) correlations. The black points are the data of EBM−, the open points are the ones of EBM+. The straight line is a fit to the points.

for cells of EBM− and in Fig. 24 for cells of EBM+ and given in Table 7. The black points are the data of BM0 which are somewhat (13%) worse.

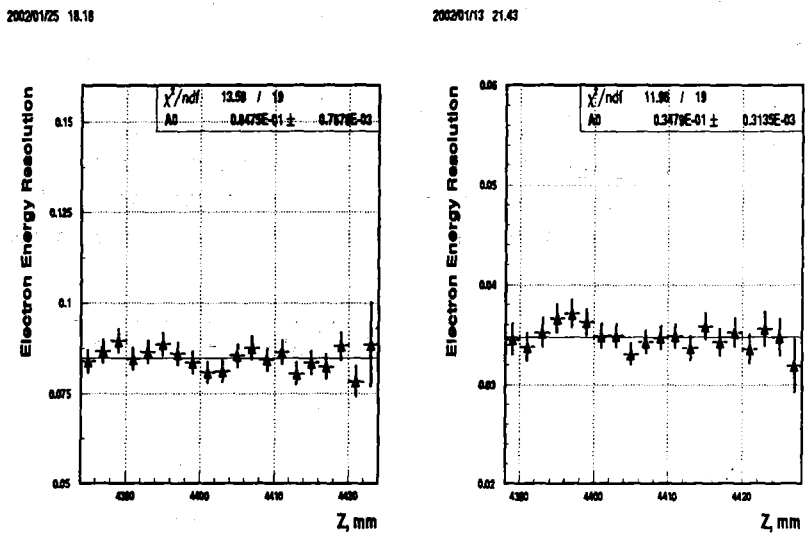

Figure 22: The electron energy resolutions, RMS/E, for $E = 20\ GeV$, EBM−, $\theta = +20°$, A−14 (left) and for $E = 180\ GeV$, EBM−, $\theta = -20°$, A−14 (right) as a function of the impact point Z coordinate.

Fit of the EBM− and EBM+ data (Fig. 25 top) by the expression

$$\frac{\sigma}{E} = \frac{a}{\sqrt{E}} + b, \tag{5}$$

produced the parameters a and b shown in Fig. 25 (bottom). As can be seen, the values of these parameters for EBM− and EBM+ agree with each other and agree with the one for the Barrel Module-0 within errors. The weighted averages for EBM− and EBM+ are equal to $a = 31.5 \pm 2.7\%$ and $b = 1.3 \pm 0.3\%$.

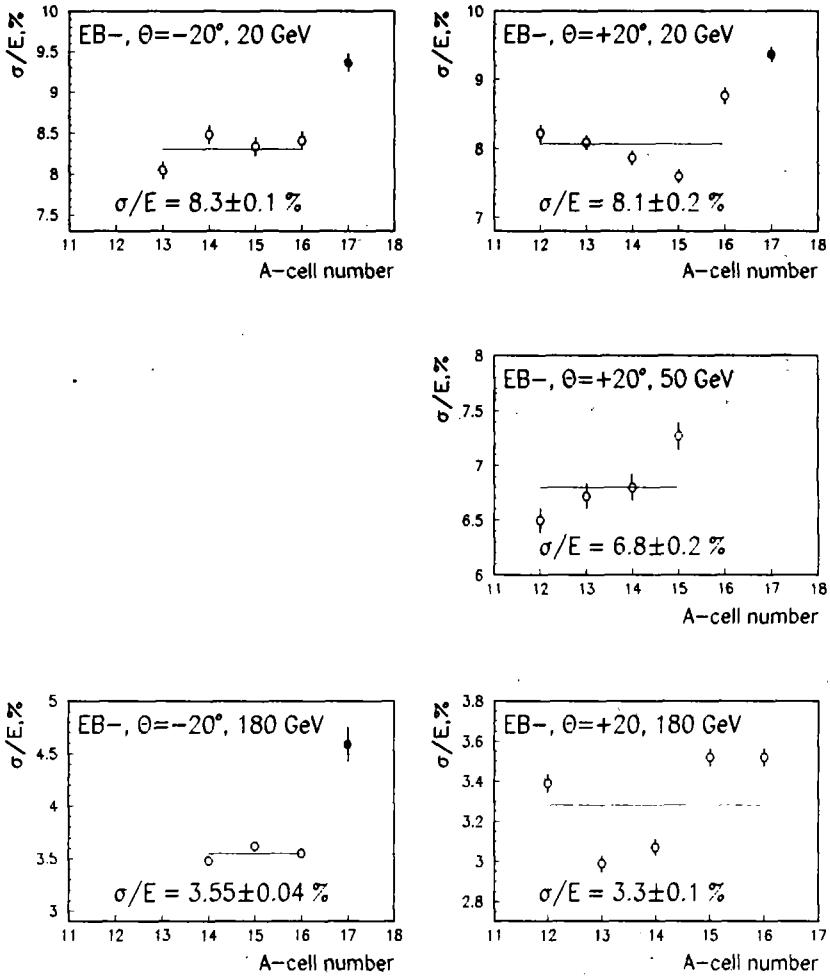

Figure 23: The electron energy resolution for the A-cells of EBM−: for $E = 20\ GeV$, $\theta = -20°$ (top-left); for $E = 20\ GeV$, $\theta = +20°$ (top-right); for $E = 50\ GeV$, $\theta = +20°$ (middle-right); for $E = 180\ GeV$, $\theta = -20°$ (bottom-left); for $E = 180\ GeV$, $\theta = +20°$ (bottom-right). The black points are the data of BM0.

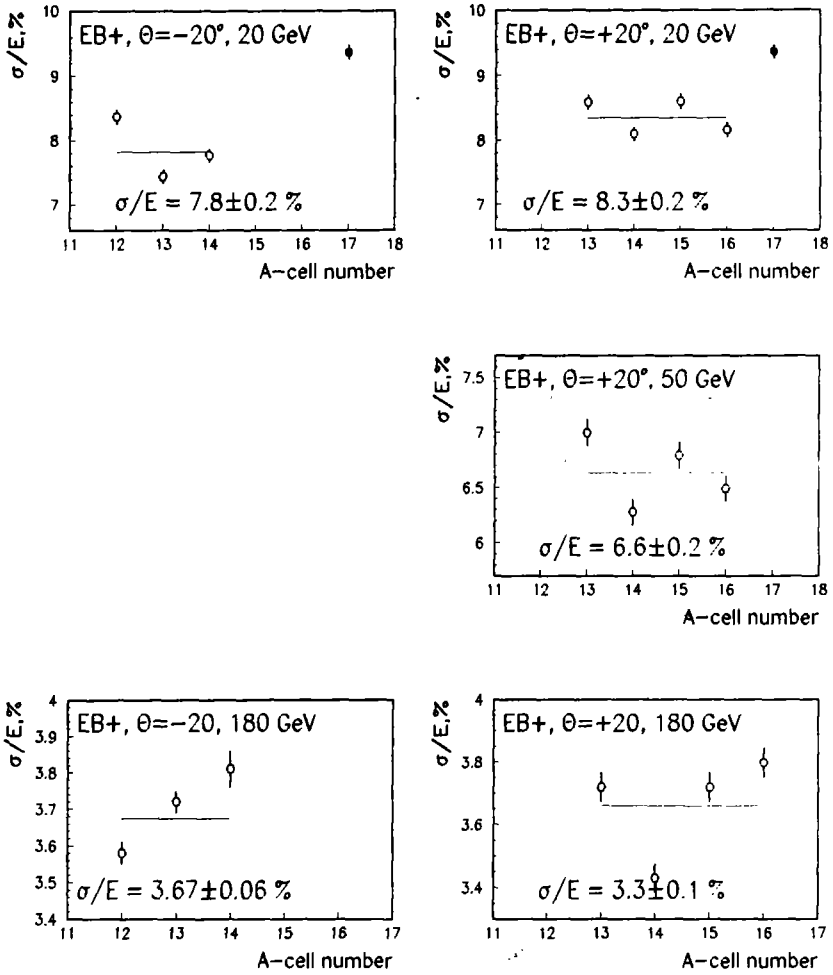

Figure 24: The electron energy resolution for cells of EBM+: for $E = 20\ GeV$, $\theta = -20^o$ (top-left); for $E = 20\ GeV$, $\theta = +20^o$ (top-right); for $E = 50\ GeV$, $\theta = +20°$ (middle-right); for $E = 180\ GeV$, $\theta = -20°$ (bottom-left); for $E = 180\ GeV$, $\theta = +20°$(bottom-right). The black points are the data of BM0.

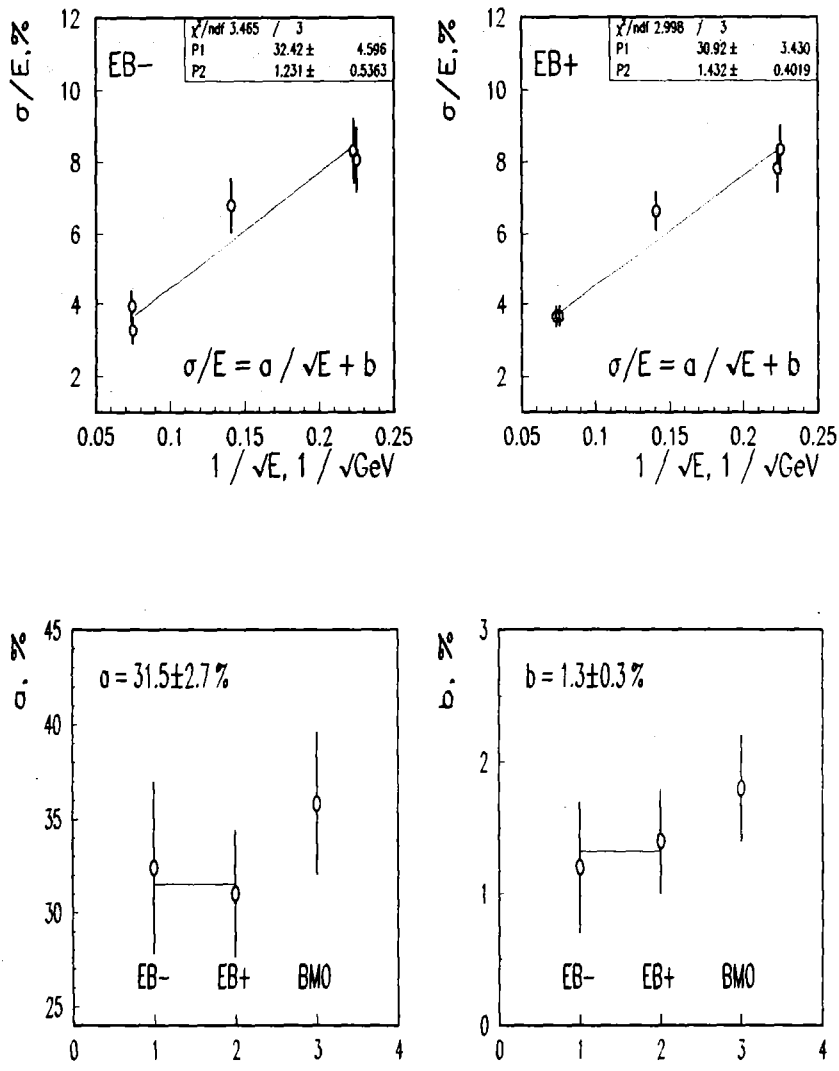

Figure 25: Top: The electron energy resolution for EBM− (left) and EBM+ (right) at $\theta = \pm 20°$ as a function of energy ($1/\sqrt{E}$). Bottom: The statistical "a" (left) and the constant "b" (right) terms of the electron energy resolution.

Table 7: The electron energy resolution (σ/E, %).

Cell	20 GeV		50 GeV	180 GeV	
	-20^o	$+20^o$	$+20^o$	-20^o	$+20^o$
A+12	8.4±0.1		6.4±0.1*	3.6±0.03	
A+13	7.4±0.1	8.6±0.1	7.0±0.1	3.7±0.03	3.7±0.03
A+14	7.8±0.1	8.1±0.1	6.3±0.1	3.8±0.05	3.4±0.03
A+15		8.6±0.1	6.8±0.1		3.7±0.03
A+16		8.2±0.1	6.5±0.1		3.8±0.03
mean	7.8±0.2	8.3±0.2	6.6±0.2	3.7±0.1	3.7±0.1
A−12		8.2±0.1	6.5±0.1		3.4±0.03
A−13	8.0±0.1	8.1±0.1	6.7±0.1		3.0±0.03
A−14	8.5±0.1	7.9±0.1	6.8±0.1	3.5±0.03	3.1±0.03
A−15	8.3±0.1	7.6±0.1	7.3±0.1	3.6±0.03	3.5±0.03
A−16	8.4±0.1	8.8±0.1		3.6±0.03	3.5±0.03
mean	8.3±0.1	8.1±0.2	6.8±0.2	3.6±0.04	3.3±0.1

* the σ/E value for -20^o

6.2 The Energy Resolution for various η

Fig. 26 shows the electron energy resolution as a function of η. The one at 180 GeV for EBM+ for $1.05 < \eta < 1.35$ is (2.79 ± 0.13) % and for EBM− for $-1.35 < \eta < -1.05$ is (2.53 ± 0.11) %.

Fig. 27 shows the one as a function of energy for $\eta = -1.35$ for extended barrel modules (September 2001 testbeam) and for $\eta = 0.45$ for barrel module 0 (July 1999 testbeam). The obtained parameterization for EBM− at $\eta = -1.35$ is

$$\sigma/E = (30 \pm 1)\%/\sqrt{E} + (0.2 \pm 0.1)\% \; . \qquad (6)$$

6.3 The Energy Resolution at $\theta = 90^o$

Fig. 28 shows the electron energy resolution as a function of a tile number. The weighted averages for EBM for $-11 < tile < -1$ at 180 GeV is

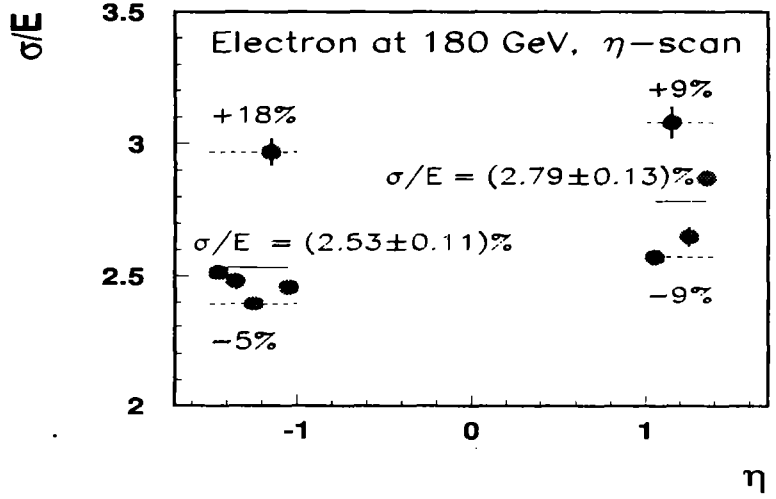

Figure 26: The electron energy resolution as a function of η for E = 180 GeV.

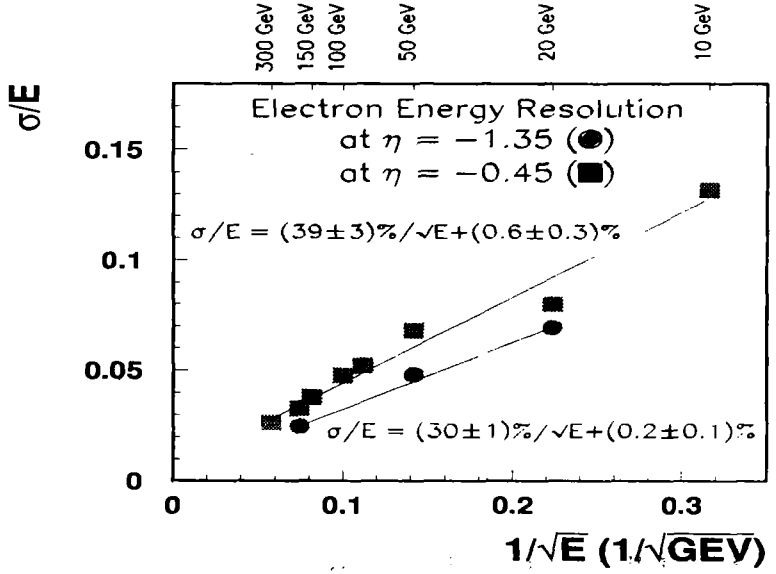

Figure 27: The electron energy resolution for $\eta = -0.45$ and $\eta = -1.35$ as a function of energy.

(2.40±0.07) %, at 20 GeV is (7.0±0.1) % and for EBM+ for $1 < tile < 11$ at 180 GeV is (2.44 ± 0.07) %, at 20 GeV is (6.8 ± 0.1) %.

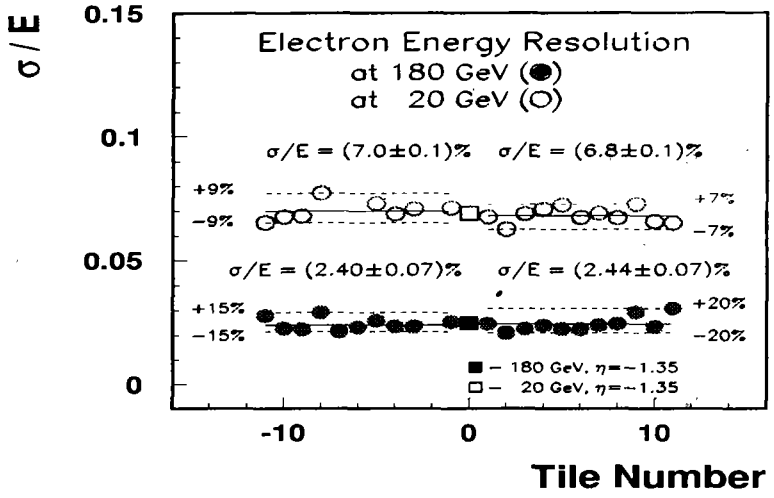

Figure 28: The electron energy resolution as a function of a tile number.

7 Pion Calibration

Since the TILECAL is a hadronic calorimeter, an important question is its calibration using hadron beams. Unfortunately, in the given setup the significant (about 10 %) part of energy leaks out. We have tried to solve this problem by the following way.

We have reconstructed the energies of pions using the e/h method suggested in [14]:

$$E_\pi = \frac{1}{e} \cdot \frac{e}{\pi} \cdot R_\pi, \tag{7}$$

where e is an electron calibration constant, R_π is the pion response,

$$\frac{e}{\pi} = \frac{e/h}{1 + (e/h - 1) \cdot f_{\pi^0}}, \tag{8}$$

$e/h = 1.36 \pm 0.01$ [15] and $f_{\pi^o} = 0.11 \cdot \ln E_{beam}$. The values of the electron calibration constants for the different modules and energies have been determined by averaging of the data given in Tables 2, 3.

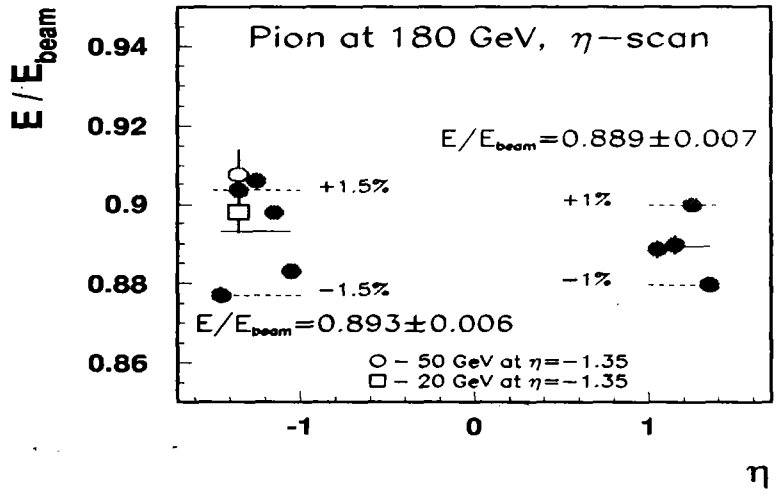

Figure 29: The normalized pion energy as a function of η for 180 GeV (black circles), 50 GeV (open circles) and 20 GeV (squares).

Fig. 29 shows the normalized pion energy (E/E_{beam}) as a function of η. The mean one for $1.05 < |\eta| < 1.35$ at 180 GeV is equal to 0.89 ± 0.01. The ones for 20 and 50 GeV agree with this value within the errors.

Fig. 30 shows the normalized pion energy as a function of a tile number. The mean ones are: at 20 GeV for $2 < tile < 10$ is 0.91 ± 0.01, at 180 GeV for $2 < tile < 10$ is 0.93 ± 0.01.

Fig. 31 shows the pion energy resolution as a function of η. The mean ones for 180 GeV for EBM− and EBM+ are equal to (6.0 ± 0.3) % and comparable with the value expected from the required overall physics performance [4] $\sigma/E = 50\%/\sqrt{E} \oplus 3\%$.

Fig. 32 shows the pion energy resolution as a function of a Tile number. The mean ones for $2 < tile < 10$ for EBM− and EBM+ are equal to (12.6 ± 0.4) % for 20 GeV and (6.50 ± 0.02) % for 180 GeV.

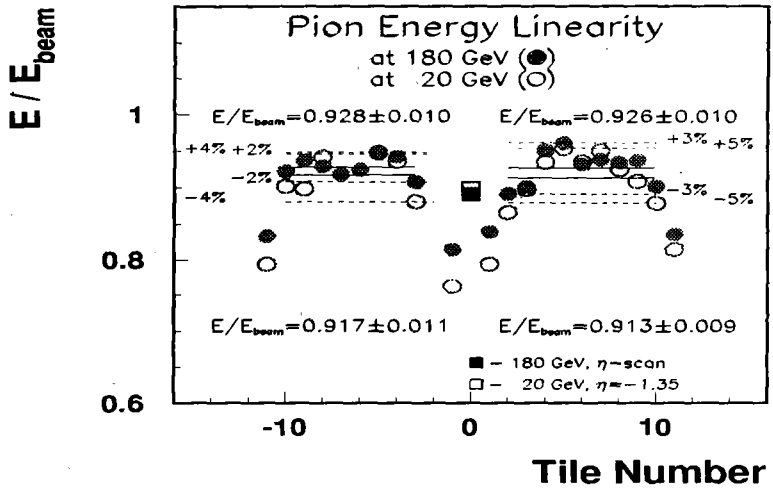

Figure 30: The normalized pion energy (E/E_{beam}) as a function of a tile number for 180 GeV (black circles) and 20 GeV (open circles). The data for η-scan for 180 GeV (black squares) and 20 GeV (open squares) are also given.

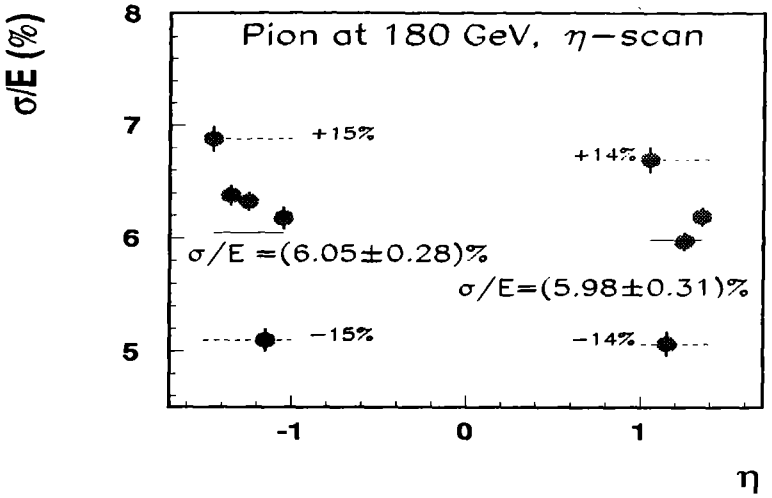

Figure 31: The pion energy resolution as a function of η.

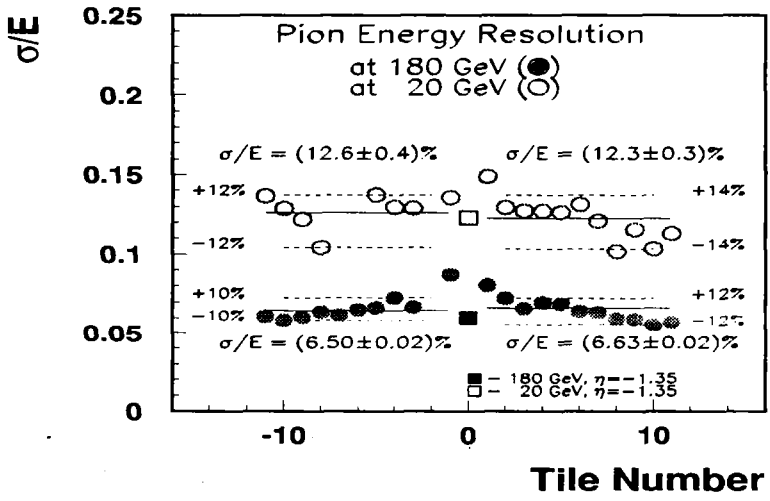

Figure 32: The pion energy resolution as a function of a tilerow number.

8 The e/h Ratio

An important characteristic of a calorimeter is the e/h ratio, an intrinsic non-compensation of one. For our calorimeter this value is equal to $e/h = 1.36 \pm 0.01$ [15] and as suggested in [16] may be used for the calorimeter calibration. We have tested such possibility in the case of a single module.

The relation between the e/h ratio and the e/π ratio is

$$\frac{e}{h} = \frac{e}{\pi} \cdot \frac{f_{\pi^o} - 1}{(e/\pi) \cdot f_{\pi^o} - 1} \tag{9}$$

$$\frac{e}{\pi} = \frac{R_e}{R_\pi \cdot \epsilon}, \tag{10}$$

where R_e is the electron response, $\epsilon = E_{beam}/E_\pi$ is the correction factor taking into account the hadronic shower lateral leakage.

The relation between the accuracy of the e/h ratio and the one of the

e/π ratio is

$$\frac{\Delta e/h}{e/h} = \frac{\Delta e/\pi}{e/\pi} \cdot \sqrt{1 + \left(\frac{f_{\pi^o} \cdot e/\pi}{1 - f_{\pi^o} \cdot e/\pi}\right)^2}. \tag{11}$$

In particular, for 180 GeV this relation equals to

$$\frac{\Delta e/h}{e/h} \approx 4 \cdot \frac{\Delta e/\pi}{e/\pi}. \tag{12}$$

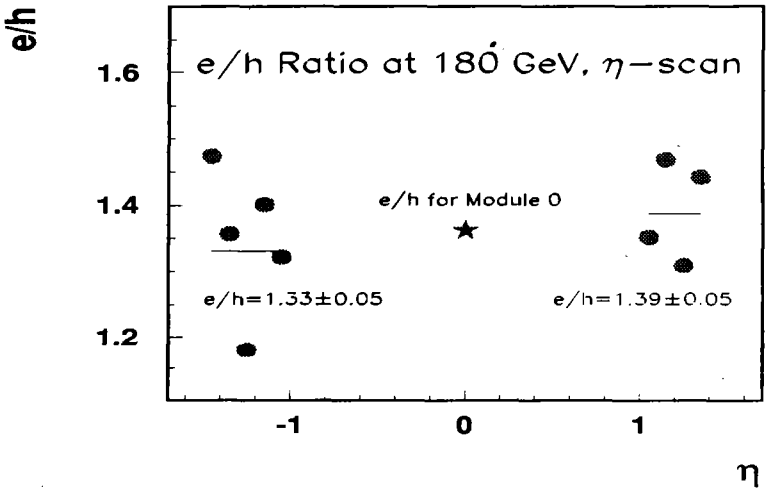

Figure 33: The e/h ratio as a function of η at 180 GeV.

Fig. 33 shows the e/h ratio as a function of η at 180 GeV. The mean ones are equal to 1.33 ± 0.05 for EBM− and 1.35 ± 0.05 for EBM+, agree with the one for BM0 and confirm the correctness of the calibration.

Fig. 34 shows the e/h ratio as a function of a tile number for 20 and 180 GeV. The mean ones are equal to 1.30 ± 0.04 for EBM− and 1.32 ± 0.04 for EBM+ for 20 GeV and 1.43 ± 0.05 for EBM− and 1.55 ± 0.05 for EBM+ for 180 GeV.

Note that, in general, the e/h ratio at $\theta = 90^o$ may be differ from the one for the module 0, obtained for the front face, due to the difference in the construction of a module from the front and lateral sides.

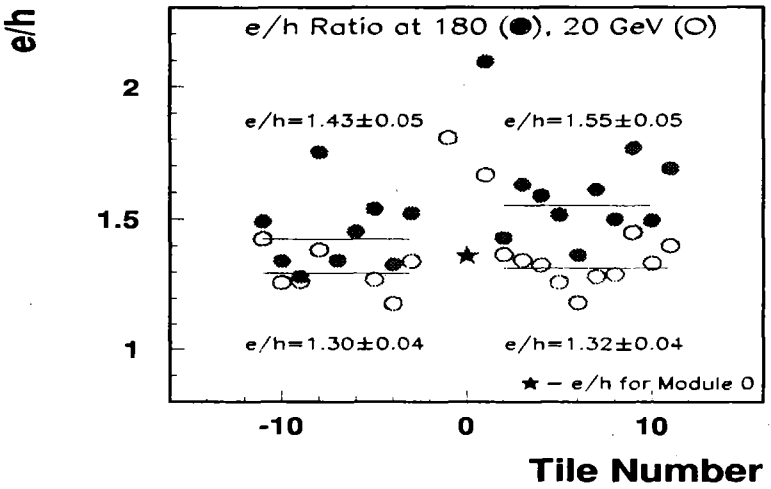

Figure 34: The e/h ratio as a function of a tile number at 20 and 180 GeV.

9 Conclusions

We have developed the method of the determination of the absolute energy scale calibration of a single module of the ATLAS TILECAL calorimeter using electron and pions of energies from 10 to 300 GeV of the CERN SPS. The method has been successfully used in the analysis of the vast data of the two extended barrel modules exposed during the test beam period in September 2001. These modules have been exposed at energies E = 20, 50, 180 GeV at $\theta = \pm 20°$ and 90° and $1.05 < |\eta| < 1.35$.

The electron calibration constants for each A-cell for each energy and angle have been determined. Their spreads as a function of cell are ±2 % for EBM− and ±3 % for EBM+. The obtained weighted averages are equal to 1.140 ± 0.007 pC/GeV for 50 and 180 GeV and 1.046 ± 0.007 pC/GeV for 20 GeV.

For the tile scan the correlation between the electron constants and the Cs and muon constants have been observed. The correlation coefficients are about of 0.7.

The obtained RMS values of the cell-to-cell uniformity of the modules are equal to 1 - 2% and the ones for the tilerow-to-tilerow uniformity are 4% and coincide with the corresponding muon data.

The electron energy resolution have been studied. The one for each A-cell for each energy and angle have been obtained. The weighted average statistical and constant terms of the expression $\sigma/E = a/\sqrt{E} + b$ for EBM− and EBM+ are equal $a = 31.5 \pm 2.7\%$ and $b = 1.3 \pm 0.3\%$ and agree with the one for the Barrel Module-0.

The method of the pion calibration of a single module has been suggested. This method uses the electron calibration constants and the known e/h ratio. The mean energy, deposited in a single module at η scan, is equal to 0.89 ± 0.01 %. The good ($\pm 1\%$) energy linearity is observed.

The measurement of the e/h ratio as one of the calibration constants has been performed. The obtained values agree with the one for BM0 and confirm the correctness of the calibration.

10 Acknowledgements

This work is the result of the efforts of many people from the ATLAS TILECAL Collaboration. The authors are greatly indebted to all Collaboration for their test beam setup and data taking. The authors are thankful to R. Leitner for valuable discussions and important comments. We acknowledged to I. Korolkov for providing the numerical data of the Cs and muon calibrations and for fruitful discussions.

References

[1] ATLAS Collaboration, ATLAS Technical Proposal, CERN/LHCC/94-43, 1994, CERN.

[2] ATLAS Collaboration, ATLAS Detector and Physics Performance, Technical Design Report, ATLAS TDR 15, CERN/LHCC/99-15.

[3] ATLAS Collaboration, ATLAS Detector and Physics Performance, Technical Design Report, ATLAS TDR 14, CERN/LHCC/99-14.

[4] ATLAS Collaboration, ATLAS Calorimeter Performance, ATLAS TDR 1, CERN/LHCC/96-40, 1996, CERN.

[5] ATLAS Collaboration, ATLAS TILE Calorimeter Technical Design Report, ATLAS TDR 3, CERN/LHCC/96-42, 1996, CERN.

[6] E. Starchenko et al., Cesium Monitoring System for ATLAS Tile Hadron Calorimeter, Poster presented at 8th Int. Conf. on Instrumentation for Colliding Beam Physics, Novosibirsk, Russia, Mart 2002; ATL-TILECAL-2002-003, CERN.

[7] J.A. Budagov et al., Radioactive sources for ATLAS hadron tile calorimeter calibration, JINR-E13-97-104, Dubna, Russia, 1997.

[8] J. Seixas et al., A remote neural discriminator for the scintillating tile calorimeter, Proc. of the 8 Int. Conf. on Calorimetry in High Energy Physics, p. 618, Lisbon, 1999.

[9] P. Amaral et al., NIM A443 (2000) 51.

[10] P. Amaral et al., Eur.Phys.J. C20 (2001) 487.

[11] J.A. Budagov, Y.A. Kulchitsky et al., Electron response and e/h ratio of Atlas Barrel Hadron Prototype Calorimeter, ATL-TILECAL-96-72 (1996) CERN, Geneva, Switzerland; JINR-E1-95-513 (1995) JINR, Dubna, Russia.

[12] O. Norniella, I. Korolkov, Comparison of Cs and 90^o muons 2001 TB data, Talk given on the analysis TILECAL meeting, February 2002, CERN;
O. Norniella, I. Korolkov, Summary of module response to Sc and muons for EB and barrel modules in 2000 and 2001 TBs, Talk given on the analysis TILECAL meeting, October 2002, CERN.

[13] R. Leitner, ATLAS Tile Calorimeter, Talk given on the ATLAS plenary meeting, October 2002, CERN.

[14] Y.A. Kulchitsky et al., The e/h method of an energy reconstruction for a combined calorimeter, ATL-TILECAL-99-025, 1999, CERN, Geneva; JINR-E1-99-317 (1999) JINR, Dubna, Russia.

[15] J.A. Budagov, Y.A. Kulchitsky et al., The e/h ratio of the Atlas Hadronic Tile Calorimeter, ATL-TILECAL-2001-001, CERN, Geneva; JINR-E1-2002-13 (2002) JINR, Dubna, Russia.

[16] Y.A. Kulchitsky, Measurement of the e/h Constant for Production Modules, Talk given on the Calibration TILECAL meeting, May 2001, CERN.

Received on February 5, 2003.